JOURNAL OF SYNCHROTRON RADIATION
ISSN 1600-5775

Effects of temperature, mechanical motion and source positional jitter on the resolving power of beamline 02B at the SSRF

Zhi Guo,‡ Xiangyu Meng,‡ Yong Wang,* Haigang Liu,* Xiangzhi Zhang, Zhongliang Li, Lian Xue and Renzhong Tai*

Shanghai Synchrotron Radiation Facility, Shanghai Institute of Applied Physics, Chinese Academy of Sciences, 239 Zhangheng Road, Pudong New District, Shanghai, People's Republic of China.
*Correspondence e-mail: wangyong@sinap.ac.cn, liuhaigang@sinap.ac.cn, tairenzhong@sinap.ac.cn

Received 12 January 2017
Accepted 22 April 2017

Edited by J. F. van der Veen

‡ These authors contributed equally to this work.

Keywords: variable-line-spacing grating; mechanical vibration; source positional jitter; energy-resolving power.

A detailed analysis of the effects of temperature excursions, instrumental mechanical motion and source position jitter on the energy-resolving power of beamline 02B at the Shanghai Synchrotron Radiation Facility (SSRF) is presented in this study. This beamline uses a bending-magnet-based source and includes a variable-line-spacing grating monochromator with additional optics. Expressions are derived for the monochromator output photon energy shifts for each of the performance challenges considered. The calculated results indicate that measured temperature excursions of ±1 K produce an energy shift of less than 11% of the system's energy resolution. Mechanical displacements and vibrations measured at amplitudes of less than 0.5 µm produce changes of less than 5%, while measured source location jitter results in a change of less than 10%. Spectroscopic test experiments at 250 and 400 eV provide energy resolutions of over 10^4. This analysis, combined with the measured results, confirms the operational stability of the beamline, indicating that it meets the performance requirements for experimental use.

1. Introduction

The Shanghai Synchrotron Radiation Facility (SSRF) is China's first third-generation synchrotron light source. Its 3.5 GeV storage ring is supplied with electrons from a 150 MeV linac through a full energy 0.15–3.5 GeV booster synchrotron. In addition to an initial complement of seven beamlines, six supplementary beamlines have recently been completed, and another two beamlines from the SiP·ME^2 (Shanghai Integrated Platform of Materials, Energy and Environment) project were completed in 2016. The implementation of third-generation synchrotrons requires that further attention be paid to monitor external mechanical motion induced by temperature changes and physical vibrations and to supervise electron bunch positional jitter. Analysis of the effects of such fluctuations is crucial in beamline design and construction. To meet the necessary requirements to operate sophisticated optical systems, it is essential to adopt sufficient countermeasures to attenuate these problematic variations and supply a stable beam. Consequently, researchers have focused intently upon these issues (Fukuda *et al.*, 1996; Sakae *et al.*, 1997; Hansen *et al.*, 1988; Matsui *et al.*, 2003; Wang *et al.*, 2008, 2009; Igarashi *et al.*, 2008; Bu *et al.*, 2008; Li *et al.*, 2011; Tang *et al.*, 2010, 2012; Tanaka *et al.*, 2002).

Understanding the many causes of the vibrations and displacements that reduce performance is critical. The SSRF is

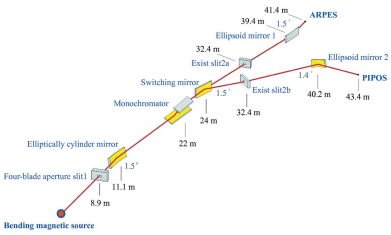

more susceptible to these issues than other select synchrotron facilities that are constructed on rock or other relatively stable geological structures. Specific sophisticated countermeasures have been applied to the SSRF to counteract these issues, *e.g.* magnet girder assemblies (Wang *et al.*, 2008) to maintain instrument stability. Hansen *et al.* (1988) identified vibrations from a number of sources, including acoustic waves, ground motion, scanning system operations, and motions coupled with experimental equipment such as pumps, fans and other motors, all of which contribute to the degradation of resolution and performance. Igarashi *et al.* (2008) found that the liquid-nitrogen cooling system for the double-crystal monochromator shook the experimental floor, which strongly affected the X-ray stability at the Photon Factory. It has been found that shutting down turbomolecular pumps during beamline operation and implementing an X-ray stability feedback system can be beneficial. Li *et al.* (2011) researched vibration sources in the Canadian Light Source and revealed many associated sources, including a fan coil system, turbomolecular pump, chiller and cryostat system. The cryostat was discovered to significantly affect the scanning transmission X-ray microscopy imaging quality. Temperature control measures in the machine tunnel were found to reduce the electron orbital drift during operation (Tanaka *et al.*, 2002). Positional displacements of synchrotron radiation instruments induced by temperature excursions also affect performance metrics such as energy-resolving power. In addition to external vibrations, electron beam orbit fluctuations with a vertical amplitude of several micrometres also affect beamline performance (Matsui *et al.*, 2003). To attenuate the effects of external and source vibrations on beamline performance, these effects should be analyzed thoroughly; the countermeasures implemented to suppress the effects will depend on the analysis results.

One of the most important beamline performance metrics is the energy-resolving power. In this paper, we analyze the effects of temperature variations, mechanical vibration and source displacement on the resolving power. Variable-line-spacing gratings (VLSGs) disperse short-wavelength light into a spectrum in addition to focusing the light onto the exit slit. They can serve as monochromators with the advantage of not requiring an exit-slit focusing mirror. This increases the available photon flux at the sample and eliminates aberrations. VLSGs are used in the 02B Ambient Pressure Photon Emission Spectroscopy (APPES) and the 03I Angle Resolved Photon Emission Spectroscopy (ARPES) beamlines at the SSRF. The measured photon flux at the APPES sample position is greater than 10^{11} photons s^{-1} (0.1% bandwidth)$^{-1}$.

During the design and construction of these beamlines, to confirm the energy resolution ($E/\Delta E$), the effects of temperature, external vibrations and source displacements were analyzed and evaluated.

2. Effects of temperature, vibrations and beam jitter on the energy-resolving power of beamline 02B at the SSRF

2.1. Description of the 02B beamline

The 02B beamline at the SSRF is under the auspices of the SiP·ME^2 project, which is the single largest undertaking conducted by the National Natural Science Foundation of China. In this project, the first of its kind in the world, the MBE/laser MBE, ARPES, STM/STS and AP-PES/PIPOS will be combined into an integrated platform to further the study of the electronic structures of new energy-related environmentally friendly materials. This platform is capable of *in situ* as well as *in operando* electronic structure measurement of materials with ultra-high resolution and is expected to offer the highest level of integration and the best overall performance in electronic structure research. The project includes both the 02B beamline described herein, which uses a bending-magnet (BM) radiation source, and the 03I beamline, which uses an elliptically polarized undulator.

Fig. 1 shows a diagram of the 02B beamline. The lead-out angle of the front-end (the angle between the beam and the linear section of the storage ring) is 1°. The four-blade slit (slit1) is located 8.855 m downstream of the BM source, which defines the acceptance angle of the beamline and is adjustable with photon energy variation. An elliptically curved cylindrical mirror for meridian focusing with a grazing-incidence angle of 1.5° is located 11.088 m downstream of the source. The beam is focused on the exit slits [slit2a for the APPES branch or slit2b for the photon-in/photon-out-spectroscopy (PIPOS) branch] in the horizontal direction. Three VLSGs in the monochromator are located 22 m downstream of the

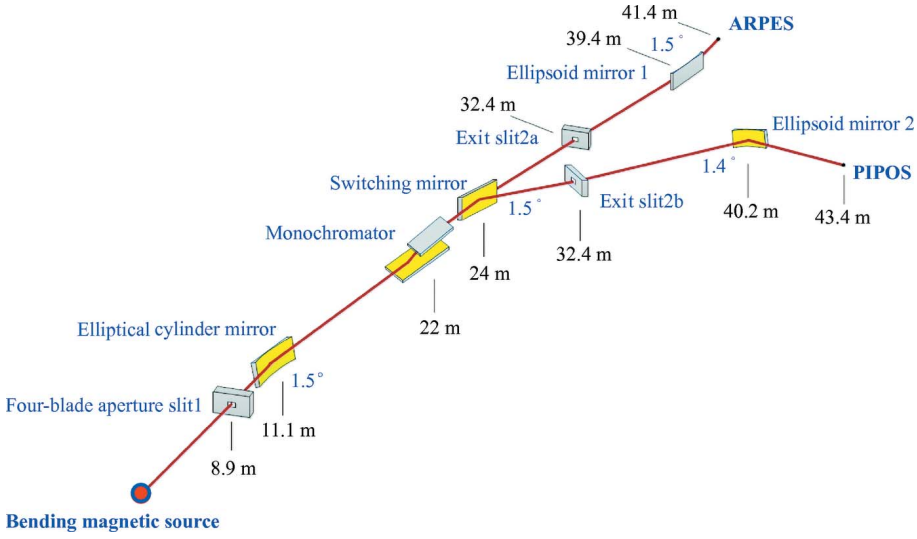

Figure 1
Optical layout of the APPES beamline of the SiP·ME^2 project.

source. The gratings have an average line spacing of 400 lines mm^{-1} to cover 40–600 eV and 800 and 1100 lines mm^{-1} spacings to cover 200 eV–2 keV and are selected to optimize their calculated resolving power and photon flux density at the sample. In addition to this dispersive function, the gratings also focus monochromatic light in the vertical direction onto the exit slits. Downstream of the switching mirror, the beamline is divided into the APPES and PIPOS endstation branches. The ellipsoidal mirrors follow the slits to focus the beam onto the sample positions of APPES (41.4 m) and PIPOS (43.4 m downstream of the source).

The monochromator is shown in Fig. 2. Its primary internal mechanisms are the motorized and water-cooled grating and plane mirror cradles, which allow the gratings and plane mirror to be rotated and translated to absorb the heat load from the synchrotron beam. The monochromator is supported by four steel vibration-isolated legs resting on a granite slab base. Granite is employed due to its low thermal expansion coefficient of 3×10^{-6} K^{-1}, compared with 1.5×10^{-5} K^{-1} for steel.

Temperature excursions will affect the height of the monochromator and exit slits and will thus change the output energy; in addition, vibrations from the floor and supports, as well as source positional jitter, will modify both the output energy and resolving power. Consequently, the contributions from temperature, ground vibrations and source jitter will be discussed below in detail.

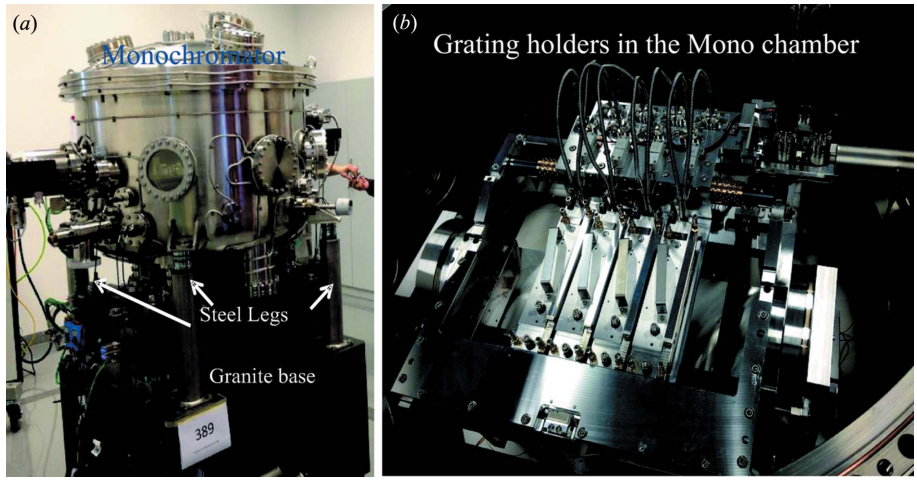

Figure 2
Monochromator of the 02B beamline. (*a*) The structures that support the internal mechanisms of the monochromator, which include the granite base and steel legs, and (*b*) the grating holders in the monochromator chamber.

2.2. Output energy variation originating from temperature change

As shown in Fig. 3, the thermal expansion of the steel and granite support structures can raise the height of the gratings, their accompanying mirrors and the exit slits uniformly. The energy deviation *versus* temperature variation can be calculated accordingly.

The new angles α' and β' are

$$\beta' = \beta + \left\{\left[D_{\text{steel}}\,\Delta T\,H_{\text{slit}} - \left(D_{\text{steel}}\,\Delta T\,H_{\text{mono-steel}} + D_{\text{granite}}\,\Delta T\,H_{\text{mono-granite}}\right)\right]/L_{\text{grating-slit}}\right\},$$
$$\alpha' = \alpha, \qquad (1)$$

where D_{steel} and D_{granite} are the expansion coefficients of steel and granite, respectively, ΔT is the temperature increase, and H_{slit}, $H_{\text{mono-steel}}$ and $H_{\text{mono-granite}}$ are the heights of the exit slit, the steel legs and the granite base of the monochromator, respectively.

If the height increase of the monochromator is Δh, the projection equation of the plane mirror on the x–y plane is

$$y = \left(x - X_{\text{Mhit}} + \frac{\Delta h}{\tan\theta}\right)\tan 2\theta. \qquad (2)$$

The projection equation of the grating on the x–y plane is

$$y - (Y_{\text{c}} + \Delta h) = x\tan(\pi/2 - \beta). \qquad (3)$$

Solving equations (2) and (3), the new impact point of the beam on the grating is

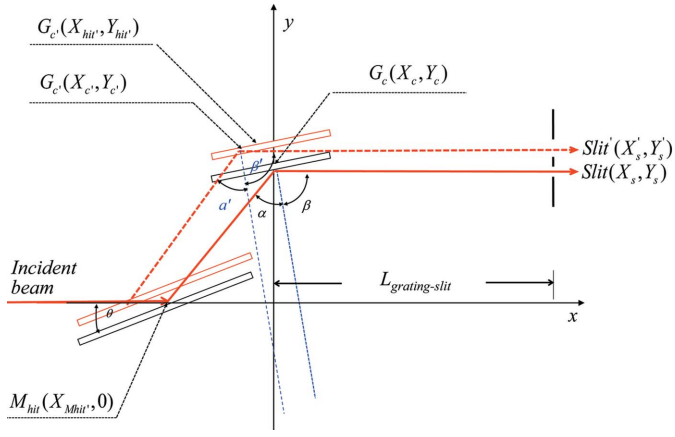

Figure 3
Coordinate system for the monochromator and exit slit. It is hypothesized that, as the temperature increases, the thermal expansion of the supporting structure (steel and granite) of the monochromator and exit slit will cause their height to increase. $G_c(X_c, Y_c)$ is the original central point position and rotational axis of the grating; $G_{c'}(X_{c'}, Y_{c'})$ is the new central point position corresponding to the increased height of the monochromator; $G_{\text{hit}}(X_{\text{hit}'}, Y_{\text{hit}'})$ is the impact point of the beam on the grating; $M_{\text{hit}}(X_{\text{Mhit}}, 0)$ is the impact point of the beam on the plane mirror; $L_{\text{grating-slit}}$ is the distance between the grating center and exit slit; Slit(X_s, Y_s) is the original coordinate position of the exit slit in the x–y coordinate plane; Slit$'(X_s', Y_s')$ is the new position corresponding to the increased height of the slit; θ is the incidence angle of the plane mirror; and α, β and α', β' are the original and new including angles of the grating. The solid and dashed lines refer to the original and current beam, respectively.

Table 1
Theoretical energy changes ΔE for the three gratings with varying temperature.

Grating	Photon energy (eV)	Energy deviation (meV) (0.5 K)	Energy deviation (meV) (1 K)	Energy deviation (meV) (5 K)	Calculated energy-resolving power (meV)
VLSG1 (400 lines mm^{-1})	250	2.1	4.2	21	36
	400	4.2	8.2	41	80
VLSG2 (1100 lines mm^{-1})	400	2.5	5	25	50
	1000	10	20	100	167
	1200	13	26	130	240
VLSG3 (800 lines mm^{-1})	400	3	6	30	57
	1000	12	24	120	222

$$X'_{\rm hit} = \frac{[1-(\tan 2\theta/\tan\theta)]\Delta h + Y_{\rm c} + X_{\rm Mhit}\tan 2\theta}{\tan 2\theta - \cot\beta}, \quad (4)$$

$$Y'_{\rm hit} = \left(x - X_{\rm Mhit} + \frac{\Delta h}{\tan\theta}\right)\tan 2\theta. \quad (5)$$

The distance between this new impact point and the grating center is

$$w = -\left[(X'_{\rm c} - X'_{\rm hit})^2 + (Y'_{\rm c} - Y'_{\rm hit})^2\right]^{1/2}. \quad (6)$$

The line density on the VLSG for the new impact point $G_{c'}(X_{c'}, Y_{c'})$ is

$$k(w) = k_0\left(1 + 2b_2 w + 3b_3 w^2 + \ldots\right). \quad (7)$$

This results in a new output energy

$$E_{\rm new} = \frac{k(w)}{\sin\alpha' - \sin\beta'}\frac{hc\times 10^3}{e}. \quad (8)$$

On the exit slit, this change in energy is represented by

$$\Delta E = E_{\rm new} - E_{\rm old}. \quad (9)$$

The lengths of the granite and steel legs are 0.6 and 0.7 m, respectively. The theoretical energy changes ΔE resulting from temperature increases of 0.5 K, 1 K and 5 K are presented in Table 1.

From these theoretical data, it is apparent that if the temperature can be controlled to within ± 1 K the energy change is maintained at 11% of the energy-resolving power (24 meV at 244 eV). The energy drift of 2 meV is negligible relative to the mechanical precision of the monochromator ($\sim$10 meV). The measured 24 h temperature variation at the SSRF is less than ± 1 K and, as such, the construction of a constant temperature hutch is unnecessary. The measured energy-resolving power is over 10^4 ($E/\Delta E$), which is equal to the theoretical resolving power. The effect of temperature variation on beamline performance is thus relatively limited and can be neglected.

2.3. Output energy variation from mechanical vibrations

Motors and other mechanical disturbances will cause the monochromator to vibrate slightly, which will induce an output energy change in addition to affecting the resolving power. Two types of sources of mechanical noise will be considered here. First, local vibrations from sources near the monochromator will rock the instrument and create height differences between the front and hind legs, causing a pitch δ of both the incident angle θ of the plane mirror and the angle $(\alpha+\beta)$ of the grating, consequently resulting in an output energy shift. Second, longer scale vibrations affecting the whole beamline will slightly dislocate the monochromator relative to the exit slits, adding an energy change and degrading the resolving power. These two cases will be discussed below.

2.3.1. Energy changes from pitching vibrations. Rocking the monochromator within the plane of the beam path rotates the optics by an angle δ as shown in Fig. 4. For modelling purposes, we take the rotation axis of the instrument as being centered on the plane mirror. The gratings will both rotate and translate from their original position slightly; thus, the impact point of the beam on the grating will shift. In these calculations, only local vibrations are considered. Because of its large distance (10.4 m) from the monochromator, the exit slit is considered to be stationary.

The beam impact point on the plane mirror is

$$X_{\rm Mhit} = -\frac{X_{\rm m}\sin\theta - Y_{\rm m}\cos\theta + R}{\sin\theta}. \quad (10)$$

The new axial position for the central rotational axis of the grating is

$$\begin{aligned} X'_{\rm c} &= X_{\rm Mhit} + \left(Y_{\rm c}^2 + X_{\rm Mhit}^2\right)^{1/2}\cos(2\theta+\delta), \\ Y'_{\rm c} &= \left(Y_{\rm c}^2 + X_{\rm Mhit}^2\right)^{1/2}\sin(2\theta+\delta). \end{aligned} \quad (11)$$

The projection of the grating on the x–y plane is

$$y - Y'_{\rm c} = (x - X'_{\rm c})\tan[(\pi/2) - \beta + \delta] = \frac{(x - X'_{\rm c})}{\tan(\beta-\delta)}. \quad (12)$$

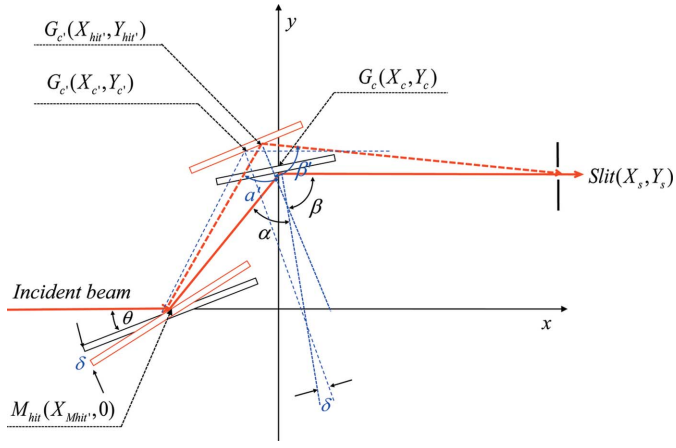

Figure 4
Diagram of output energy changes associated with rocking of the monochromator. The pitch angle δ results from the height difference between the front and hind legs.

The reflected beam off the plane mirror is given by

$$y = (x - X_{\rm Mhit})\tan(2\theta + 2\delta). \quad (13)$$

Subsequently, the new beam impact point on the grating is found by solving (4) and (5),

$$X'_{\rm hit} = \frac{\tan(\beta-\delta)\tan(2\theta+2\delta)X_{\rm Mhit} + Y'_{\rm c}\tan(\beta-\delta) - X'_{\rm c}}{\tan(\beta-\delta)\tan(2\theta+2\delta) - 1}, \quad (14)$$

$$Y'_{\rm hit} = \frac{\tan(2\beta+2\delta)\left[Y'_{\rm c}\tan(\beta-\delta) + X_{\rm Mhit} - X'_{\rm c}\right]}{\tan(\beta-\delta)\tan(2\theta+2\delta) - 1}. \quad (15)$$

Then, the new angles α' and β' for the gratings are

$$\beta' = \beta - \delta + \arctan\left(\frac{Y_{\rm S} - Y'_{\rm hit}}{X_{\rm S} - X'_{\rm hit}}\right), \quad (16)$$

$$\alpha' = \pi - 2(\theta+\delta) - (\beta - \delta). \quad (17)$$

The distance between the incident beam center on the grating and the grating center is

$$w = -\left[(X'_c - X'_{\rm hit})^2 + (Y'_{\rm c} - Y'_{\rm hit})^2\right]^{1/2}. \quad (18)$$

The grating line density at the new location of the incident beam center is represented by

$$k(w) = k_0\left(1 + 2b_2 w + 3b_3 w^2 + \ldots\right). \quad (19)$$

The new output energy at the exit slit is

$$E_{\rm new} = \frac{k(w)}{\sin\alpha' - \sin\beta'}\frac{hc\times 10^3}{e}. \quad (20)$$

Finally, the energy change is given by

$$\Delta E = E_{\rm new} - E_{\rm old}. \quad (21)$$

The calculated energy changes for the 400 lines mm^{-1} and 1100 lines mm^{-1} grating spacings are illustrated in Fig. 5. The base vibration of the SSRF experimental hall has an amplitude of less than 0.4 µm, as shown in Fig. 8; the energy change will be less than one-tenth of the energy resolution, which is negligible.

2.3.2. Energy changes from height differences between the monochromator and exit slit. A second type of monochromator motion in the plane of the beam path is an overall rise or heave, wherein the elevation of the monochromator increases by Δh while the height of the exit slit remains stable, as shown in Fig. 6.

With a rise Δh in height, the diffraction angles α' and β' become

$$\beta' = \beta - \arctan\left(\Delta h / L_{\rm grating\text{-}slit}\right), \quad (22)$$

$$\alpha' = \alpha. \quad (23)$$

The projection of the plane mirror on the x–y plane is

$$y = \left(x - X_{\rm Mhit} + \frac{\Delta h}{\tan\theta}\right)\tan 2\theta. \quad (24)$$

Solving the relationships above for the impact point of the incident beam on the gratings gives

$$X'_{\rm hit} = \frac{[1 - (\tan 2\theta/\tan\theta)]\,\Delta h + Y_{\rm c} + X_{\rm Mhit}\tan 2\theta}{\tan 2\theta - \cot\beta}, \quad (25)$$

$$Y'_{\rm hit} = \left(x - X_{\rm Mhit} + \frac{\Delta h}{\tan\theta}\right)\tan 2\theta. \quad (26)$$

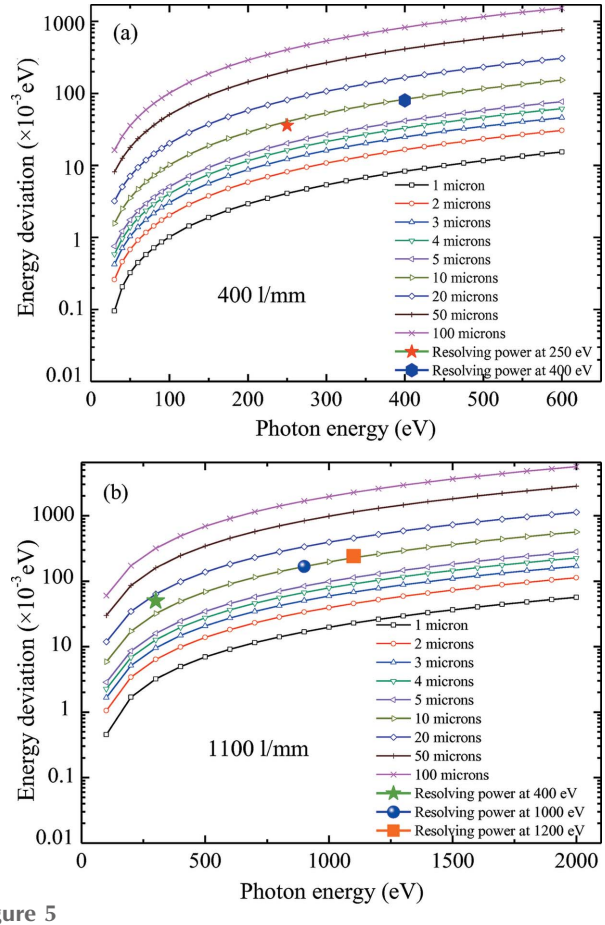

Figure 5
Theoretical energy change originating from monochromator vibrations for (*a*) a grating spacing with a central line density of 400 lines mm^{-1} and (*b*) a grating spacing with a central line density of 1100 lines mm^{-1}.

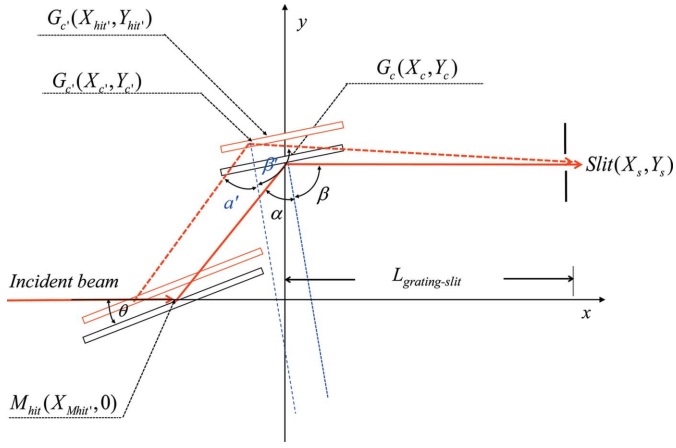

Figure 6
Diagram of energy changes caused by a heave between the monochromator and exit slit.

The distance between the grating center and impact point is

$$w = -\left[(X_c' - X_{hit}')^2 + (Y_c' - Y_{hit}')^2\right]^{1/2}. \quad (27)$$

The energy changes for the two grating spacings of 400 lines mm^{-1} and 1100 lines mm^{-1} induced by whole-body monochromator vibrations are illustrated in Fig. 7. The vibration amplitude of SSRF is less than 0.4 µm, as shown in Figs. 8 and 9; the energy change will be less than 5% of the energy resolution.

Fig. 8 displays the results of four days of RMS vertical displacement measurements for the monochromator base. Based on the analysis above, the effects of vertical displacements will be less than 5% of the resolving power, which is negligible relative to the mechanical precision of monochromator energy scanning.

Fig. 9 shows the spectrum of the RMS vertical vibrations at the base of the monochromator. In the frequency range from 10 mHz to 20 Hz, the vertical displacement of the ground base at night is noticeably smaller by a factor of 2 to 4 relative to that during the daytime. Most vibrations in this frequency range originate from terrestrial forces, such as tidal oscillations along the oceanic coastline approximately 20 km from the facility and human activities (*e.g.* automobile motion and human movements).

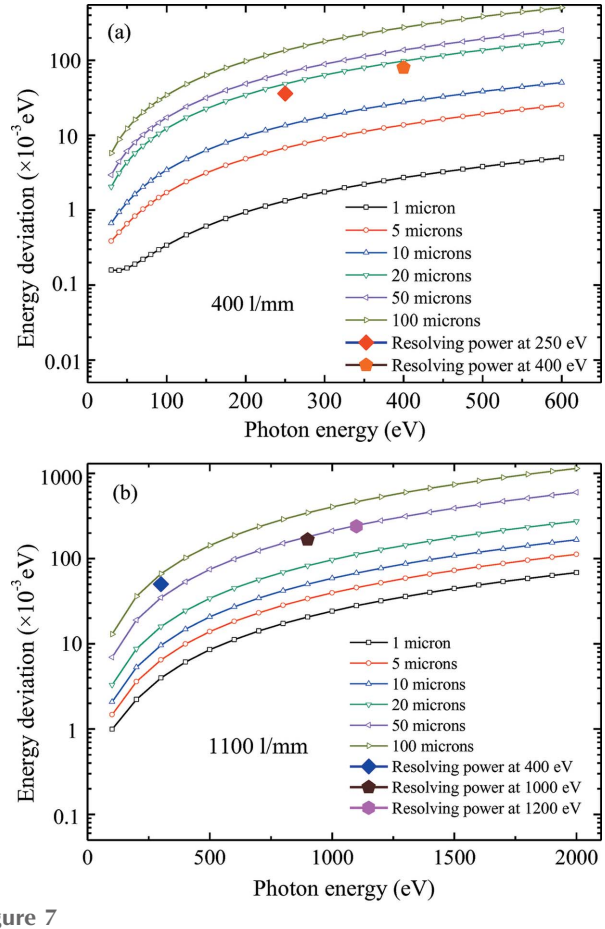

Figure 7
Theoretical energy changes from the monochromator heave for the 400 lines mm^{-1} grating (*a*) and the 1100 lines mm^{-1} grating (*b*).

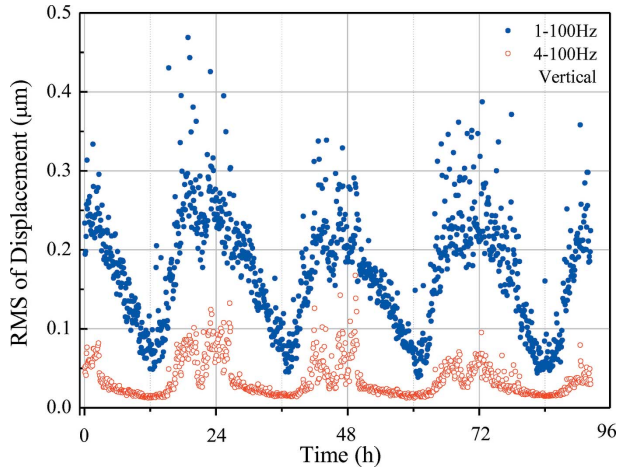

Figure 8
Measured RMS vertical vibration amplitude at the base of the monochromator.

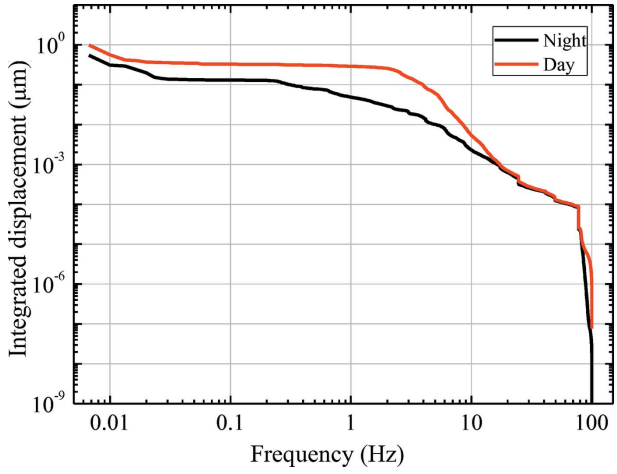

Figure 9
Measured RMS vertical vibration spectrum for the base of the monochromator.

2.4. Energy changes caused by source positional jitter

Variations in the location of the electron bunches in the bending magnet will also affect the output energy and resolution. As illustrated in Fig. 10, changes in the source location cascade through the monochromator optics system by changing the beam path.

If the source moves along the vertical direction by a height change Δh, and if the distance between the source and four-blade aperture (Slit1) is L_{ss1}, then the new incident angle on the plane mirror is given by

$$\theta' = \theta + (\Delta h / L_{ss1}). \quad (28)$$

If the distance between the source and grating is L_{sg}, then the shift of the impact point on the plane mirror is given by L, where

$$\frac{L_{sg} + X_{Mhit} - L_{ss1}}{\sin(\pi - \theta')} = \frac{L}{\sin(\Delta h / L_{ss1})}. \quad (29)$$

Therefore, L is represented by

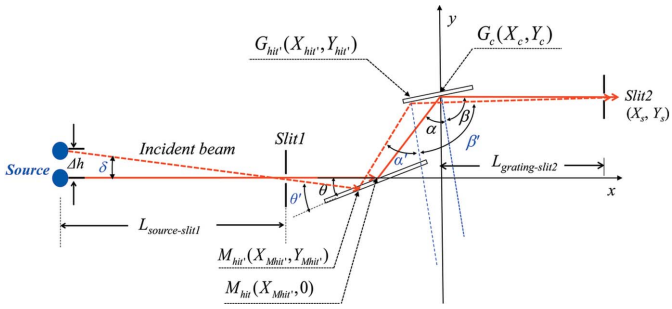

Figure 10
Diagram of beam path changes resulting from source displacement.

$$L = \frac{\left(L_{sg} + X_{Mhit} - L_{ss1}\right)\sin(\Delta h/L_{ss1})}{\sin\theta'}. \quad (30)$$

The coordinates of the new impact point on the plane mirror are

$$X'_{Mhit} = X_{Mhit} - L\cos\theta, \quad (31)$$

$$Y'_{Mhit} = -L\sin\theta. \quad (32)$$

The projection of the beam reflected off the plane mirror onto the x–y plane is

$$y - Y'_{Mhit} = \tan\left[2\theta' - (\Delta h/L_{ss1})\right](x - X'_{Mhit}). \quad (33)$$

The projection of the grating onto the x–y plane is

$$y - Y_c = (x - X_c)\cot\beta. \quad (34)$$

The impact point of the reflected beam on the grating is

$$X'_{hit} = \frac{\tan\left[2\theta' - (\Delta h/L_{ss1})\right]X'_{Mhit} - Y'_{Mhit} + Y_c - X_c\cot\beta}{\tan\left[2\theta' - (\Delta h/L_{ss1})\right] - \cot\beta}, \quad (35)$$

$$Y'_{hit} = X'_{hit}\cot\beta + Y_c. \quad (36)$$

The new incident and diffraction angles α' and β' are given by

$$\beta' = \beta + \arctan\left(\frac{Y_c - Y'_{hit}}{L_{gs2}}\right), \quad (37)$$

$$\alpha' = \pi - 2\theta' - \beta'. \quad (38)$$

The distance between the impact point on the grating and the grating center is

$$w = -\left[(X'_c - X'_{hit})^2 + (Y'_c - Y'_{hit})^2\right]^{1/2}. \quad (39)$$

The energy change can be subsequently obtained similar to equations (19) to (21).

The source-displacement-induced energy changes for the two grating spacings of 400 lines mm^{-1} and 1100 lines mm^{-1} are shown in Fig. 11. If the magnitude of the source displacement is less than 3 µm, the energy change will be less than one-quarter of the resolving power. Fig. 12 illustrates electron bunch position data over 24 h of SSRF operation. With a vertical displacement jitter of less than 0.8 µm, as shown in Fig. 12, the energy changes will be less than 5% of the energy resolution and are consequently considered unimportant.

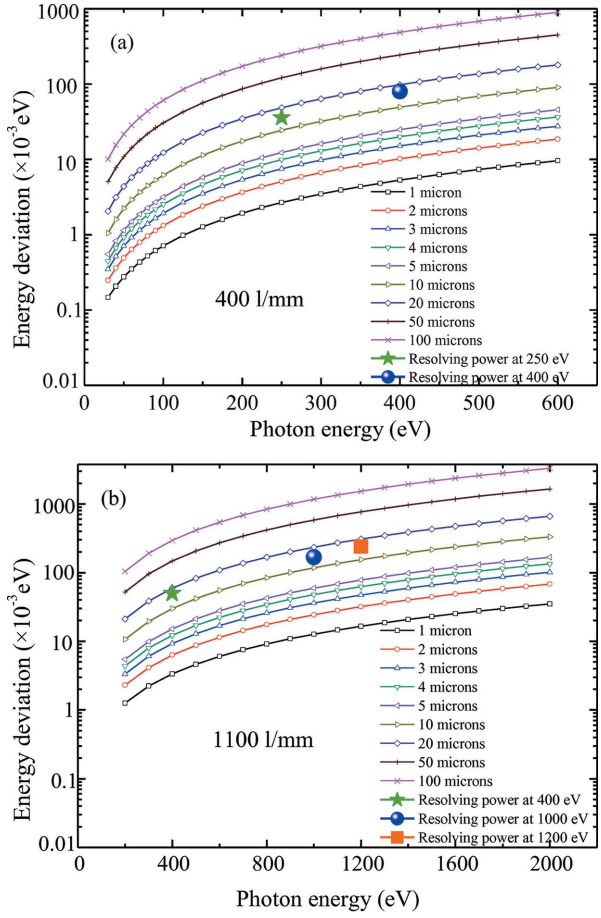

Figure 11
Output energy changes from vertical source displacements for the (*a*) 400 lines mm^{-1} and (*b*) 1100 lines mm^{-1} grating spacings.

3. Experimental results

An ionization chamber was installed downstream of the exit slit to measure the energy resolution for the beamline by recording shell excitation spectra of N_2 and Ar (see Figs. 13 and 14, respectively). The gas pressure in the ionization chamber was approximately 1×10^{-6} Torr. An accelerating grid of gold mesh and a microchannel plate detector were

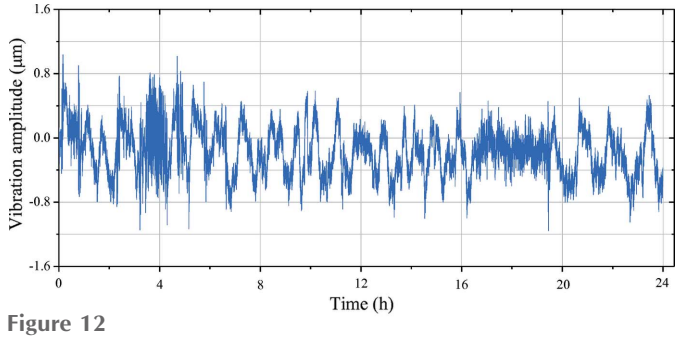

Figure 12
Measured vertical electron bunch displacements in the storage ring of the SSRF over a 24 h period.

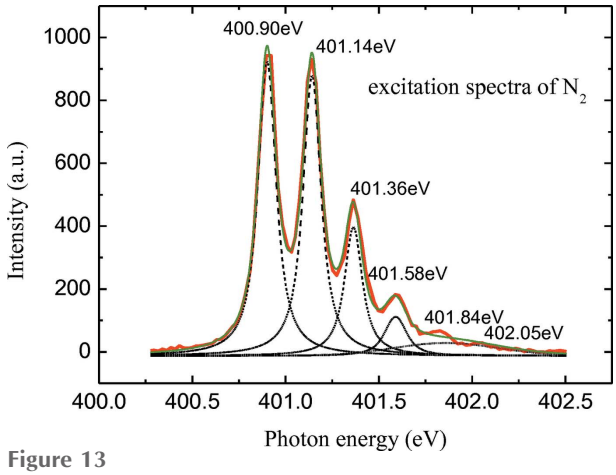

Figure 13
Excitation spectrum of N_2 gas measured using the ionization chamber downstream of the exit slit. The energy-resolving power is 1.05×10^4 at 400.9 eV.

placed on top of the beam to collect and amplify the gas ion signals. Previous studies employing this configuration (Xue *et al.*, 2010) discussed how the energy-resolving power ($E/\Delta E$) could be obtained. The Ar $L_{2,3}$ absorption-edge transitions to Rydberg levels $2p_{3/2}^{-1} \rightarrow nl$ and $2p_{1/2}^{-1} \rightarrow nl$, and the fine structure resonances $2p_{3/2} \rightarrow 4s$, $3d$, $4d$, $5d$, $6d$, $7d$ and $2p_{1/2} \rightarrow 4s$, $3d$, $4d$, $5d$, $6d$ were observed. The line shape is a Voigt profile, a convolution of a naturally broadened Lorentzian with an instrumental Gaussian. The energy-resolving power is $E/\Delta E = E/\Gamma_G$, where Γ_G is the Gaussian broadening. From an analysis of the Ar excitation spectra at 244.2 eV, the Gaussian width Γ_G is 23 meV ± 3 meV, resulting in a resolving power of 1.05×10^4. Measurements of N_2 at 400.9 eV also give a resolving power of 1.05×10^4, at which the photon flux is 4×10^{10} photons s^{-1} (0.1% bandwidth)$^{-1}$ with a storage-ring current of 300 mA operating at 3.5 GeV.

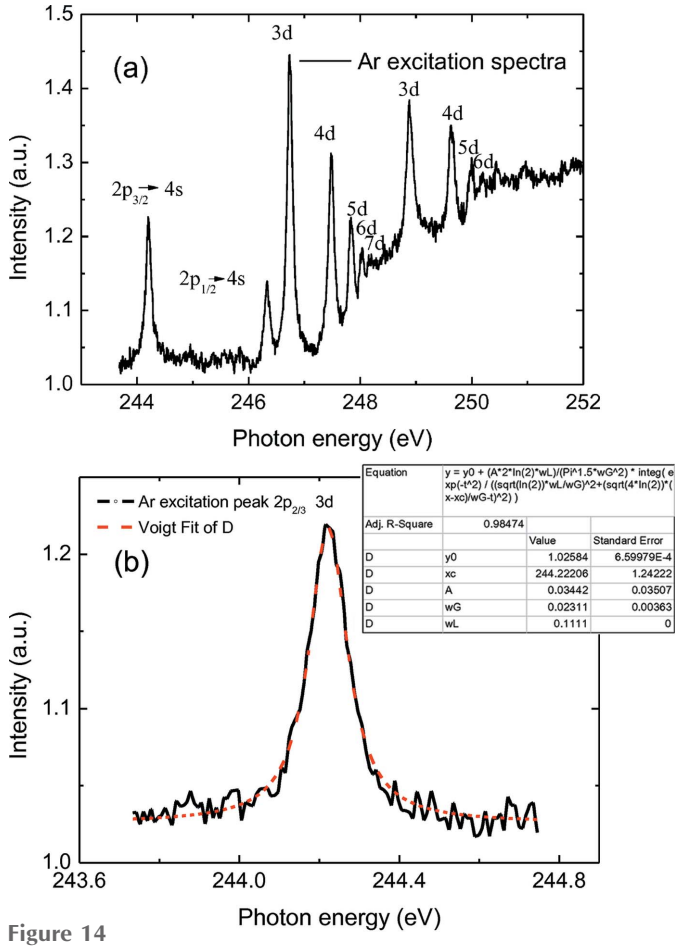

Figure 14
(*a*) Excitation spectra of Ar gas from 243.7 eV to 252 eV. (*b*) Detail of the $2p_{3/2} \rightarrow 4s$ resonance at 244.2 eV; the resolving power is 1.06×10^4.

Although the source in this beamline is a BM, the resolving power is somewhat higher than the undulator beamline BL08U at the SSRF (Xue *et al.*, 2010). The photon flux and energy stability have been very good during our testing period of over six months. It is evident from the analyses conducted herein that the effects of temperature excursions, mechanical vibrations and source jitter on the energy-resolving power are within acceptable limits and thus fulfill the requirements for endstation experiments.

4. Conclusion

A detailed analysis of the effects of temperature variation, instrumental component motion and source location jitter on the energy-resolving power was conducted for the 02B soft X-ray beamline of the SiP·ME^2 project at the SSRF. The derived analytical expressions are expected to be valuable for experiments employing this VLSG-based soft X-ray beamline. Temperature variations of ±1 K cause an energy drift of approximately 2 meV, which is 10% of the energy-resolving power; this value is significantly smaller than the mechanical precision of the monochromator and is thus considered negligible. Mechanical vibrations with amplitudes of less than 0.5 µm result in a change of less than 5%. Source motion of ±1 µm has an effect of less than 10%. The tested energy-resolving powers are over 10^4 at 244 eV and 401 eV, which are almost equal to the theoretical values. These results confirm that the SSRF can fulfil experimental requirements using this beamline.

Funding information

Funding for this research was provided by: National Natural Science Foundation of China (award Nos. 11575284, 1150050438, 11475251); National Major Scientific Instruments and Equipment Development of NSFC (award No. 11227902); National Key Basic Research Program of China '973 Program' (award No. 2013CB632901); Key Program of NSFC (award No. 51332002); National Key Research and Development Program (award No. 2016YFB0700404).

References

Bu, L.-S., Zhao, Z.-T., Yin, L.-X. & Du, H.-W. (2008). *Chin. Phys. C*, **32**, 37–39.
Fukuda, M., Endo, N., Tsuyuzaki, H., Suzuki, M. & Deguchi, K. (1996). *Jpn. J. Appl. Phys.* **35**, 6458–6462.

Hansen, R. W. C., Brodsky, E., Collier, S., Pruett, C. H., Salehzadeh, A., Wallace, D. & Middleton, F. (1988). *Nucl. Instrum. Methods Phys. Res. A*, **266**, 538–543.
Igarashi, N., Ikuta, K., Miyoshi, T., Matsugaki, N., Yamada, Y., Yousef, M. S. & Wakatsuki, S. (2008). *J. Synchrotron Rad.* **15**, 292–295.
Li, J. W., Matias, E., Chen, N., Kim, C.-Y., Wang, J., Gorin, J., He, F., Thorpe, P., Lu, Y., Chen, W. F., Grochulski, P., Chen, X. B. & Zhang, W. J. (2011). *J. Synchrotron Rad.* **18**, 109–116.
Matsui, S., Oishi, M., Tanaka, H., Yorita, T., Tsumaki, K., Kumagai, N. & Nakazato, T. (2003). *Jpn. J. Appl. Phys.* **42**, L338–L341.
Sakae, H., Aoyagi, H., Oura, M., Kimura, H., Ohata, T., Shiwaku, H., Yamamoto, S., Sugiyama, H., Tanabe, K., Kobaski, K. & Kitamura, H. (1997). *J. Synchrotron Rad.* **4**, 204–209.
Tanaka, H., Aoyagi, H., Daté, S., Fukami, K., Fukui, T., Kudo, T., Kumagai, N., Matsui, S., Nakatani, T. & Nakazato, T. (2002). *7th International Workshop on Accelerator Alignment (IWAA 2002)*, SPring-8, Japan.
Tang, S., Yin, C. & Liu, D. (2010). *High Power Laser Part. Beams*, pp. 1631–1634.
Tang, S., Yin, C. & Liu, D. (2012). *Nucl. Sci. Tech.* **23**, 7–9.
Wang, X., Cao, Y., Du, H. & Yin, L. (2009). *J. Synchrotron Rad.* **16**, 1–7.
Wang, X., Chen, L., Yan, Z., Du, H. & Yin, L. (2008). *J. Synchrotron Rad.* **15**, 385–391.
Xue, C., Wang, Y., Guo, Z., Wu, Y., Zhen, X., Chen, M., Chen, J., Xue, S., Peng, Z., Lu, Q. & Tai, R. (2010). *Rev. Sci. Instrum.* **81**, 103502.